Journal of Advanced Marine Engineering and Technology, Vol. 49, No. 6, pp. 536~542, 2025
J. Advanced Marine Engineering and Technology (JAMET)
https://doi.org/10.5916/jamet.2025.49.6.536

ISSN 2234-7925 (Print)
ISSN 2765-4796 (Online)
Original Paper

Maneuverability measure of hovering-type underwater vehicles using robotic manipulability: A preliminary study

Jin-Kyu Choi† · Hayato Kondo[1] · Shuhei Nishida[2]

(Received December 8, 2025 ; Revised December 20, 2025 ; Accepted December 20, 2025)

Abstract: Considering a mission involving the installation of seafloor instruments using an underwater vehicle, it is crucial to place the instrument at the desired location as accurately and safely as possible. However, a fixed thruster configuration may not provide sufficient performance for installing instruments of varying shapes and sizes, and modifying the thruster arrangement can compensate for this limitation. This paper applies robotic manipulability to evaluate the maneuverability of underwater vehicles when selecting a thruster arrangement suitable for accomplishing a given task. We first outline robotic manipulability and formulate the input–output velocity relationship of an underwater vehicle with n thrusters on a horizontal plane to apply the concept. We then examine the maneuverability of two thruster configurations: an equilateral-triangle arrangement composed of three thrusters and a square arrangement composed of four thrusters. Furthermore, the sum of the vector norms of the thruster speeds is computed while the vehicle tracks a straight-line path to investigate its relationship with the vehicle's maneuverability. These results demonstrate that robotic manipulability can be effectively applied to evaluating the maneuverability of underwater vehicles and that a higher level of maneuverability contributes to reducing energy consumption.

Keywords: Manipulability, Maneuverability, Thruster arrangement, Underwater vehicle, Energy saving

1. Introduction

High-precision and reliable marine observations, including crustal deformation that causes earthquakes and changes in marine ecosystems, are essential for understanding the nature and mitigation of natural disasters. To achieve this, it is crucial to install instruments at the desired location as accurately and safely as possible.

Free fall **[1]** or wire **[2]** deployment from a surface vessel has usually been used to install seafloor instruments, and a remotely operated vehicle (ROV) **[3]** or a manned submersible **[4]** has been used when the instrument is sufficiently small and lightweight. However, the free-fall method is strongly affected by ocean currents and often causes instruments to land hundreds of meters away from the intended location. ROVs and manned submersibles enable precise placement while allowing operators to check seafloor conditions; however, significant limitations remain, such as the need for continuous operator control, substantial performance variability depending on operator skill, and the requirement for heavy support equipment such as winches and cranes. These constraints reduce opportunities for deployment operations.

An autonomous underwater vehicle (AUV) provides a promising platform for accomplishing desired deployments; however, a fixed thruster configuration may not provide sufficient performance for installing instruments of varying shapes and sizes, and modifying the thruster arrangement can compensate for this limitation, as shown in **Figure 1**. This paper discusses the use of robotic manipulability to evaluate the maneuverability of underwater vehicles when selecting a thruster arrangement suitable for accomplishing a given task.

Robotic manipulability was proposed by Yoshikawa as an index for evaluating the manipulating ability of an end-effector **[5][6]**; reference **[5]** addresses the kinematic aspects, whereas **[6]** deals with the dynamic aspects. Robotic manipulability has typically been applied to manipulator systems, and its application to mobile platforms has been relatively limited; however, several studies have reported the use of dynamic manipulability in drones **[7]** and AUVs **[8]**.

† Corresponding Author (ORCID: https://orcid.org/0000-0003-3730-5900): Professor, Ocean Science & Technology School, Korea Maritime & Ocean University, 727, Taejong-ro, Yeongdo-gu, Busan 49112, South Korea, E-mail: jk-choi@kmou.ac.kr, Tel: 051-410-4342
1 Professor, Tokyo University of Marine Science and Technology, E-mail: hkondo@kaiyodai.ac.jp, Tel: +81-3-5245-7384
2 Researcher, Japan Agency for Marine-Earth Science and Technology, E-mail: shuheinishida@jamstec.go.jp, Tel: +81-46-867-9332

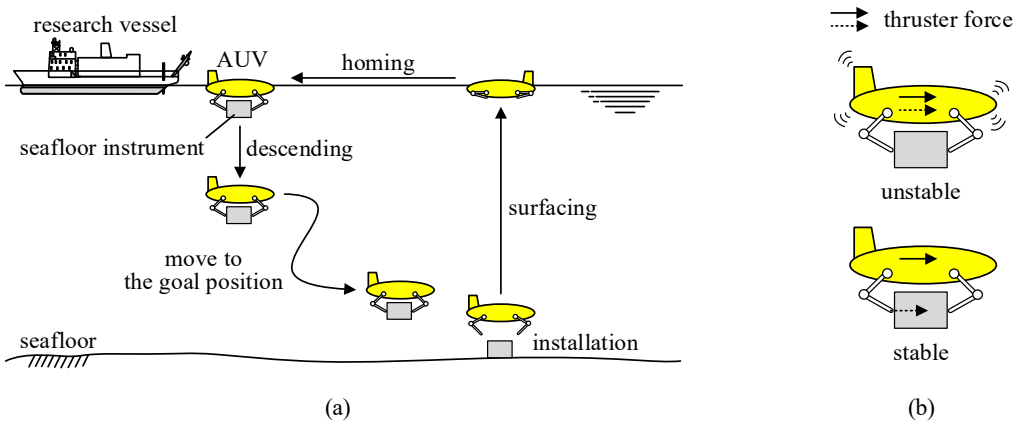

Figure 1: (a) Mission example: pinpoint installation of a seafloor instrument using an AUV. (b) Improved AUV maneuverability achieved by modifying the thruster arrangement.

In this paper, we investigate the relationship between manipulability and energy consumption during path tracking for a hovering-type AUV. Hovering-type AUVs have more thrusters than the degrees of freedom required for full motion, and this paper focuses on motion on a horizontal plane as a preliminary study. To do this, we first outline robotic manipulability in **Section 2** and formulate the input–output velocity relationship of an underwater vehicle with n thrusters in **Section 3**. **Section 4** examines the maneuverability of two thruster configurations: an equilateral-triangle arrangement composed of three thrusters and a square arrangement composed of four thrusters. Furthermore, the sum of the vector norms of the thruster speeds is computed while tracking a straight-line path. These results demonstrate that robotic manipulability can be effectively applied to evaluating the maneuverability of underwater vehicles and that a higher level of maneuverability contributes to reducing energy consumption.

2. Outline of Robotic Manipulability

Consider a robotic manipulator with n joints. Let $\boldsymbol{r} = (r_1\ r_2\ \cdots\ r_m)^T \in \Re^m$ be the positions and rotational angles of the end-effector, and let $\boldsymbol{\theta} = (\theta_1\ \theta_2\ \cdots\ \theta_n)^T \in \Re^n$ be the joint angles. Then, we have

$$\boldsymbol{r} = f(\boldsymbol{\theta}) \tag{1}$$

Differentiating **Equation (1)** with respect to time, we obtain the following input–output velocity relationship:

$$\dot{\boldsymbol{r}} = J\dot{\boldsymbol{\theta}} \tag{2}$$

where, $J = \frac{\partial f(\boldsymbol{\theta})}{\partial \boldsymbol{\theta}} \in \Re^{m\times n}$ is the Jacobian matrix, $\dot{\boldsymbol{\theta}}$ is the input to the manipulator, and $\dot{\boldsymbol{r}}$ is the output. The manipulability measure is given by

$$w = \sqrt{\det(JJ^T)} \tag{3}$$

where, det (•) is the determinant of a matrix •, $w = |\det(J)|$ if $m = n$, and $w = 0$ if $\mathrm{rank}(J) < m$.

To investigate the meaning of **Equation (3)**, we consider the case where $\|\dot{\boldsymbol{\theta}}\|^2 = \dot{\theta}_1^2 + \dot{\theta}_2^2 + \cdots + \dot{\theta}_n^2 \le 1$ is applied to the manipulator. Then, **Equation (2)** yields

$$\begin{aligned}\|\dot{\boldsymbol{\theta}}\|^2 &= \dot{\boldsymbol{\theta}}^T\dot{\boldsymbol{\theta}} \\ &= (J^{\#}\dot{\boldsymbol{r}})^T J^{\#}\dot{\boldsymbol{r}} \\ &= \dot{\boldsymbol{r}}^T(JJ^T)^{-1}\dot{\boldsymbol{r}} \le 1\end{aligned} \tag{4}$$

where, $J^{\#} = J^T(JJ^T)^{-1} \in \Re^{n\times m}$ is the pseudo-inverse of J, JJ^T is a positive semi-definite symmetric matrix, and the inverse of JJ^T exists when $\mathrm{rank}(J) = m$. Using the singular value decomposition of J, i.e., $J = U\Sigma V^T$, **Equation (4)** can be rewritten by

$$\|\dot{\boldsymbol{\theta}}\|^2 = \dot{\boldsymbol{\gamma}}^T\Sigma^{-2}\dot{\boldsymbol{\gamma}} \le 1 \tag{5}$$

where, $\dot{\boldsymbol{\gamma}} = U^T\dot{\boldsymbol{r}} \in \Re^m$, $U = (\boldsymbol{u}_1\ \boldsymbol{u}_2\ \cdots\ \boldsymbol{u}_m)^T \in \Re^{m\times m}$, $\boldsymbol{u}_i \in \Re^m$ is an eigenvector of JJ^T, $V = (\boldsymbol{v}_1\ \boldsymbol{v}_2\ \cdots\ \boldsymbol{v}_n)^T \in \Re^{n\times n}$, $\boldsymbol{v}_i \in \Re^n$ is an eigenvector of J^TJ, U and V are orthogonal

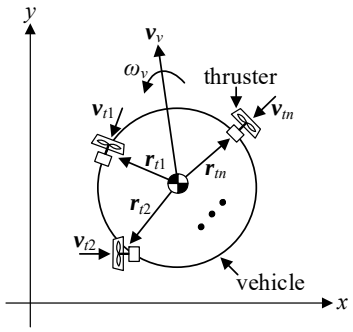

Figure 2: Schematic of an underwater vehicle with n thrusters on a horizontal plane.

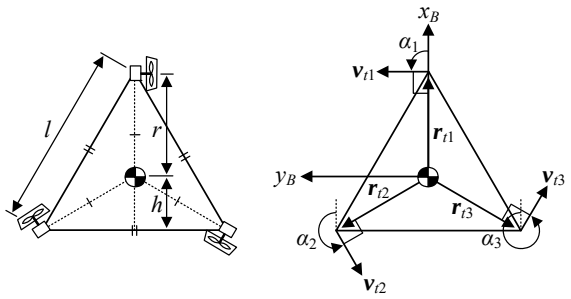

Figure 3: Three thrusters arranged in an equilateral triangle configuration.

matrices, $\Sigma = (\mathrm{diag}(\sigma_1, \sigma_2, \cdots, \sigma_m)\ \mathbf{0}_{m\times(n-m)}) \in \Re^{m\times n}$, and $\Sigma^{-2} = \mathrm{diag}(1/\sigma_1^2, 1/\sigma_2^2, \cdots, 1/\sigma_m^2)$.

Equation (5) represents the ellipsoid of $\dot{\boldsymbol{\gamma}}$ which is obtained by rotating the ellipsoid of $\dot{\boldsymbol{r}}$ by U. Here, $\sigma_1, \sigma_2, \cdots, \sigma_m$ are the lengths of the semi-axes and $\boldsymbol{u}_1, \boldsymbol{u}_2, \cdots, \boldsymbol{u}_m$ are the corresponding directions with respect to the original coordinate system. The volume of the ellipsoid is proportional to the product of the lengths of the semi-axes, i.e., $\sigma_1\sigma_2\cdots\sigma_m$ and the manipulability measure w given in **Equation (3)** is equal to this product.

3. Application to Underwater Vehicles

Figure 2 shows an underwater vehicle with n thrusters on a horizontal plane. Let $\boldsymbol{v}_v \in \Re^2$ and $\omega_v \in \Re$ be the linear and angular velocities of the vehicle, respectively, $\boldsymbol{v}_{ti} \in \Re^2$ be the linear velocity exerted by the i-th thruster, and $\boldsymbol{r}_{ti} \in \Re^2$ be the position vector from the vehicle's center of mass to the i-th thruster. The relationship between $\boldsymbol{v}_{ti}$ and $(\boldsymbol{v}_v, \omega_v)$ is given by

$$\boldsymbol{v}_{ti} = \boldsymbol{v}_v + E\boldsymbol{r}_{ti}\omega_v \tag{6}$$

where, E is the orthogonal rotation matrix rotating an arbitrary vector counterclockwise by 90° in a plane and given by

$$E = \begin{pmatrix} 0 & -1 \\ 1 & 0 \end{pmatrix} \tag{7}$$

Let $s_{ti} \in \Re$ be the speed generated by the i-th thruster and $\boldsymbol{e}_{ti} \in \Re^2$ be the direction vector of the i-th thruster. Since $\boldsymbol{v}_{ti} = s_{ti}\boldsymbol{e}_{ti}$, **Equation (6)** can be extended to the case of n thrusters as follows:

$$\begin{pmatrix} \boldsymbol{e}_{t1} & \mathbf{0} & \cdots & \mathbf{0} \\ \mathbf{0} & \boldsymbol{e}_{t2} & \cdots & \mathbf{0} \\ \vdots & \vdots & \ddots & \vdots \\ \mathbf{0} & \mathbf{0} & \cdots & \boldsymbol{e}_{tn} \end{pmatrix} \begin{pmatrix} s_{t1} \\ s_{t2} \\ \vdots \\ s_{tn} \end{pmatrix} = \begin{pmatrix} I_2 & E\boldsymbol{r}_{t1} \\ I_2 & E\boldsymbol{r}_{t2} \\ \vdots & \vdots \\ I_2 & E\boldsymbol{r}_{tn} \end{pmatrix} \begin{pmatrix} \boldsymbol{v}_v \\ \omega_v \end{pmatrix} \tag{8}$$

where, $\mathbf{0}$ is a 2×1 zero vector. Consequently, we can obtain the following input–output velocity relationship:

$$\boldsymbol{V}_v = J_t \boldsymbol{s}_t \tag{9}$$

where, $\boldsymbol{V}_v = (\boldsymbol{v}_v^T\ \omega_v)^T \in \Re^3$, $\boldsymbol{s}_t = (s_1\ s_2\ \cdots\ s_n)^T \in \Re^n$, and $J_t = B_t^{\#}E_t \in \Re^{3\times n}$, where, $B_t \in \Re^{2n\times 3}$ is the matrix on the right side of **Equation (8)** and $E_t \in \Re^{2n\times n}$ is the matrix on the left side. As a result, similar to **Equation (3)**, the maneuverability measure of the vehicle can be expressed as

$$w_t = \sqrt{\det\left(J_t J_t^T\right)} \tag{10}$$

where, $m = 3$ because we deal with the vehicle on a horizontal plane, and $w_t = |\det(J_t)|$ if $n = 3$ and $w_t = 0$ if $\mathrm{rank}(J_t) < 3$.

4. Numerical Examples

4.1 Using Three Thrusters

Figure 3 shows an equilateral triangle arrangement formed by three thrusters. Let $l = 1$ m, $r = \frac{\sqrt{3}}{3}l$, and $h = \frac{\sqrt{3}}{6}l$. The position vectors of the thrusters are given by $\boldsymbol{r}_{t1} = (r\ \ 0)^T$, $\boldsymbol{r}_{t2} = (-h\ \ \frac{l}{2})^T$, and $\boldsymbol{r}_{t3} = (-h\ \ -\frac{l}{2})^T$. Let α_i $(i = 1, 2, 3)$ be the direction angle of the i-th thruster and the x_B-y_B frame be the body frame attached to the vehicle. In the figure, $\boldsymbol{v}_{ti}$ is perpendicular to $\boldsymbol{r}_{ti}$ (denoted by $\alpha_i = \perp \boldsymbol{r}_{ti}$) and α_i is varied to investigate the resulting maneuverability.

We examine the maneuverability for the following four cases: (i) $\alpha_1 = 90^o$, $\alpha_2 = 210^o$, and $\alpha_3 = -30^o$ (i.e., $\alpha_i = \perp \boldsymbol{r}_{ti}$); (ii)

Table 1: Maneuverability w_t for the cases presented in **Subsection 4.1**. Here, $\alpha_i = \perp \boldsymbol{r}_{ti}$ denotes the angle α_i at which $\boldsymbol{v}_{ti}$ is perpendicular to $\boldsymbol{r}_{ti}$. The inequality signs indicate which value is larger.

	$\alpha_i = \perp \boldsymbol{r}_{ti}$		$\alpha_i = \perp \boldsymbol{r}_{ti} \pm 30^o$		$\alpha_i = \perp \boldsymbol{r}_{ti} \pm 45^o$		$\alpha_i = \perp \boldsymbol{r}_{ti} \pm 60^o$
w_t	0.1667	>	0.1443	>	0.1179	>	0.0833

$\alpha_i = \perp \boldsymbol{r}_{ti} \pm 30^o$; (iii) $\alpha_i = \perp \boldsymbol{r}_{ti} \pm 45^o$; (iv) $\alpha_i = \perp \boldsymbol{r}_{ti} \pm 60^o$, for $i = 1, 2, 3$. For simplicity, the three angles α_i $(i = 1, 2, 3)$ are varied by the same amount; this modification affects only on the maneuverability corresponding to the rotational velocity. The Jacobian matrix J_t in **Equation (10)** is given by

$$J_t = B_t^{\#} E_t \in \Re^{3\times 3} \tag{11}$$

$$B_t = \begin{pmatrix} I_2 & E\boldsymbol{r}_{t1} \\ I_2 & E\boldsymbol{r}_{t2} \\ I_2 & E\boldsymbol{r}_{t3} \end{pmatrix} \in \Re^{6\times 3} \tag{12}$$

$$E_t = \begin{pmatrix} \boldsymbol{e}_{t1} & \boldsymbol{0} & \boldsymbol{0} \\ \boldsymbol{0} & \boldsymbol{e}_{t2} & \boldsymbol{0} \\ \boldsymbol{0} & \boldsymbol{0} & \boldsymbol{e}_{t3} \end{pmatrix} \in \Re^{6\times 3} \tag{13}$$

where, $\boldsymbol{e}_{ti} = R(\alpha_i)(1\ \ 0)^T$ and $R(\alpha_i) = \begin{pmatrix} \cos(\alpha_i) & -\sin(\alpha_i) \\ \sin(\alpha_i) & \cos(\alpha_i) \end{pmatrix}$.

Table 1 shows the maneuverability for the four cases. It is observed that the case $\alpha_i = \perp \boldsymbol{r}_{ti}$ yields the largest value, and the maneuverability decreases as the angle deviation increases. This is because the angular velocity can be produced most effectively when $\alpha_i = \perp \boldsymbol{r}_{ti}$. To examine this in detail, we compute the singular value decomposition of J_t, i.e., $J_t = U_t \Sigma_t {V_t}^T$. At $\alpha_i = \perp \boldsymbol{r}_{ti}$, the singular value matrix Σ_t and the orthogonal matrix U_t are obtained as

$$\Sigma_t = \begin{pmatrix} 1.0000 & 0 & 0 \\ 0 & 0.4082 & 0 \\ 0 & 0 & 0.4082 \end{pmatrix} \tag{14}$$

$$U_t = \begin{pmatrix} 0 & -1 & 0 \\ 0 & 0 & -1 \\ -1 & 0 & 0 \end{pmatrix} \tag{15}$$

From the column vectors of U_t, the first diagonal component of Σ_t represents the length of the semi-axis of the ellipse associated with the rotational velocity, while the second and third components correspond to the velocities along the *x*- and *y*-axes, respectively. We observe that the maneuverability associated with rotational velocity is the largest, and the maneuverabilities associated with the linear velocities are identical. The other three cases ($\alpha_i = \perp \boldsymbol{r}_{ti} \pm 30^o, \pm 45^o, \pm 60^o$) show the same pattern, and the singular values corresponding to the rotational velocity are 0.8660, 0.7071, and 0.5000 for $\perp \boldsymbol{r}_{ti} \pm 30^o$, $\pm 45^o$, and $\pm 60^o$, respectively. This thruster configuration is advantageous for motions that require frequent rotations. To verify this property, we perform simulations of straight-line path tracking while varying the path angle θ_p shown in **Figure 4**.

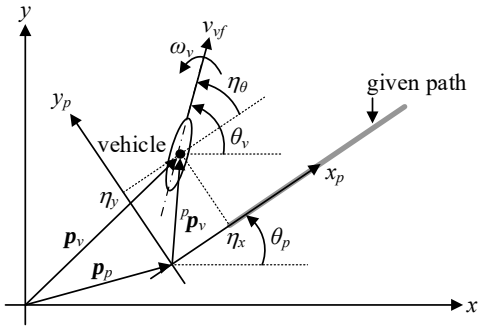

Figure 4: Notations for tracking a straight-line path.

Figure 4 shows the notations for tracking a straight-line path. Let $\boldsymbol{p}_v$, $\boldsymbol{p}_p$, and $^p\boldsymbol{p}_v = (\eta_x\ \eta_y)^T$ be the position vectors of the vehicle, the origin of the x_p-y_p frame (path frame) with respect to the fixed frame, and the vehicle with respect to the path frame, respectively. Let v_{vf} be the forward speed of the vehicle and θ_v, θ_p, and η_θ be the heading angle of the vehicle, the angle of the x_p-axis measured from the x-axis, and the angle of the forward direction measured from the x_p-axis, respectively. The path-tracking objective can be achieved by making η_y and η_θ equal to zero.

From **Figure 4**, the linear and rotational velocities of the vehicle with respect to the fixed x-y frame are given by

$$\begin{pmatrix} \dot{x}_v \\ \dot{y}_v \\ \dot{\theta}_v \end{pmatrix} = \begin{pmatrix} \cos(\theta_v) & 0 \\ \sin(\theta_v) & 0 \\ 0 & 1 \end{pmatrix} \begin{pmatrix} v_{vf} \\ \omega_v \end{pmatrix} \tag{16}$$

and v_{vf} and ω_v are obtained by

$$v_{vf} = v_{vfd} \tag{17}$$

$$\omega_v = -k_y \eta_y - k_\theta \eta_\theta \tag{18}$$

Table 2: Sum of the vector norms of the thruster speeds $\boldsymbol{s}_t$ (denoted by $\Sigma||\boldsymbol{s}_t||$) for the cases presented in **Subsection 4.1** when tracking the straight-line path with path angle θ_p, as shown in **Figure 5**.

	$\alpha_i = \perp \boldsymbol{r}_{ti}$		$\alpha_i = \perp \boldsymbol{r}_{ti} \pm 30^o$		$\alpha_i = \perp \boldsymbol{r}_{ti} \pm 45^o$		$\alpha_i = \perp \boldsymbol{r}_{ti} \pm 60^o$
$\Sigma\|\|\boldsymbol{s}_t\|\|$ at $\theta_p = 20^o$	487.9322	<	488.0926	<	488.4120	<	489.3600
$\Sigma\|\|\boldsymbol{s}_t\|\|$ at $\theta_p = 40^o$	489.3361	<	489.9522	<	491.1661	<	494.6763
$\Sigma\|\|\boldsymbol{s}_t\|\|$ at $\theta_p = 60^o$	491.5318	<	492.8354	<	495.3684	<	502.4738

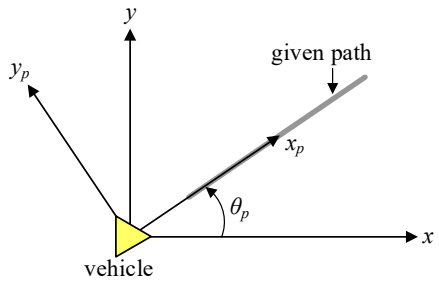

Figure 5: A straight-line path used for the simulations. The sum of the vector norms of $\boldsymbol{s}_t$ is computed as the path angle θ_p varies.

where, k_y and k_θ are control gains, v_{vfd} is the desired forward speed of the vehicle, and η_y and η_θ are computed by

$$\begin{pmatrix}\eta_x \\ \eta_y\end{pmatrix} = {}^p\boldsymbol{p}_v = R^T(\theta_p)(\boldsymbol{p}_v - \boldsymbol{p}_p) \tag{19}$$

$$\eta_\theta = \theta_v - \theta_p \tag{20}$$

The actual control input $\boldsymbol{s}_t$ in **Equation (9)** is obtained as follows. First, the linear velocities with respect to the fixed frame, $(\dot{x}_v \;\; \dot{y}_v)^T$, obtained by **Equation (16)** are transformed into the linear velocities with respect to the body frame, $\boldsymbol{v}_v$, using $\boldsymbol{v}_v = R^T(\theta_v)(\dot{x}_v \;\; \dot{y}_v)^T$. Next, compute $\boldsymbol{s}_t = J_t^{-1}\boldsymbol{V}_v$. Then, apply $\boldsymbol{s}_t$ to **Equation (9)** to obtain $\boldsymbol{v}_v$. Consequently, the motion of the vehicle can be computed using $(\dot{x}_v \;\; \dot{y}_v)^T = R(\theta_v)\boldsymbol{v}_v$ and $\dot{\theta}_v = \omega_v$.

Figure 5 shows the simulation conditions. The vehicle starts from the stationary position $(0 \;\; 0)^T$ m with a heading angle of 0°. The parameters are set to $v_{vfd} = 1$ m/s, $k_y = 1$, and $k_\theta = 1.2$. The sum of the vector norms of the thruster speeds $\boldsymbol{s}_t$ is examined as the path angle θ_p is varied to 20^o, 40^o, and 60^o. Since the simulation results for all four cases follow the same pattern, the case $\alpha_i = \perp \boldsymbol{r}_{ti}$ is presented as a representative example. **Figure 6** shows the results. It is observed that a larger

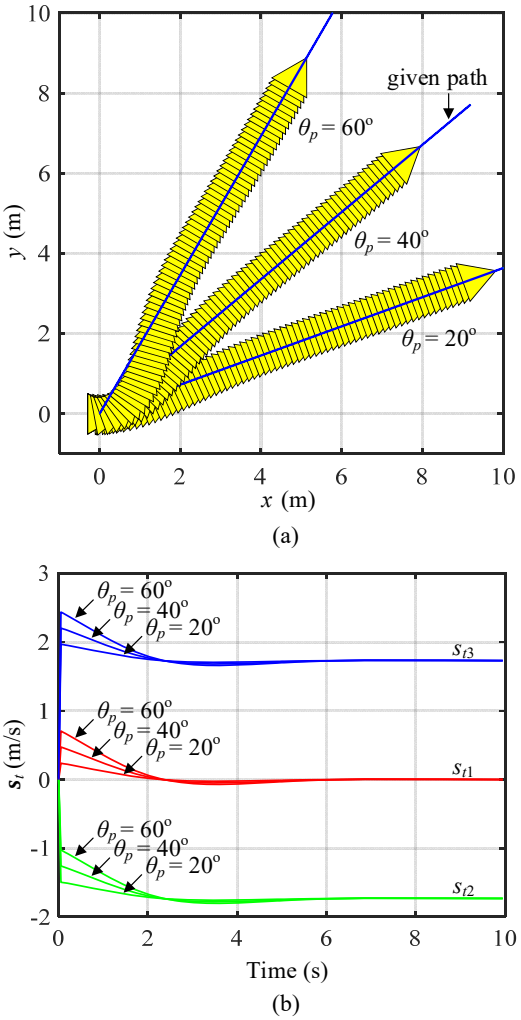

Figure 6: Simulation results of straight-line path tracking for the case $\alpha_i = \perp \boldsymbol{r}_{ti}$. (a) Position and heading angle. (b) Thruster speeds $\boldsymbol{s}_t$.

path angle θ_p requires a higher thruster speeds $\boldsymbol{s}_t$ to produce the increased rotational motion (this trend can also be seen in **Table 2**). **Table 2** presents the sum of the vector norms of $\boldsymbol{s}_t$ (denoted by $\Sigma||\boldsymbol{s}_t||$) for all cases. In contrast to the maneuverability results, the case $\alpha_i = \perp \boldsymbol{r}_{ti}$ yields the smallest value, and $\Sigma||\boldsymbol{s}_t||$ increases as the angle deviation becomes larger. This implies that

Table 3: Sum of the vector norms of the thruster speeds $\boldsymbol{s}_t$ (denoted by $\Sigma||\boldsymbol{s}_t||$) for the cases presented in **Subsection 4.2** when tracking a straight-line path with path angle θ_p. The case $\alpha_i =\perp \boldsymbol{r}_{ti}$ (shorter) corresponds to the example shown in **Figure 9**.

	$\alpha_i =\perp \boldsymbol{r}_{ti}$		$\alpha_i =\perp \boldsymbol{r}_{ti} \pm 30^o$		$\alpha_i =\perp \boldsymbol{r}_{ti} \pm 45^o$	$\alpha_i =\perp \boldsymbol{r}_{ti}$ (shorter)
w_t	0.0884	>	0.0765	>	0.0625	0.1250
$\Sigma\|\|\boldsymbol{s}_t\|\|$ at $\theta_p = 20^o$	563.6932	<	563.9696	<	564.5191	563.2764
$\Sigma\|\|\boldsymbol{s}_t\|\|$ at $\theta_p = 40^o$	566.1011	<	567.1498	<	569.2034	564.4983
$\Sigma\|\|\boldsymbol{s}_t\|\|$ at $\theta_p = 60^o$	569.8188	<	572.0021	<	576.2011	566.4225

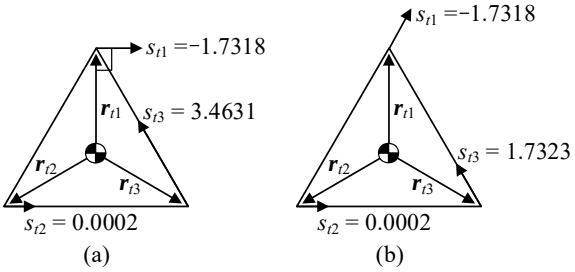

Figure 7: Thruster speeds $\boldsymbol{s}_t$ when the vehicle exactly tracks the straight line. (a) $\alpha_1 =\perp \boldsymbol{r}_{t1}$, $\alpha_2 =\perp \boldsymbol{r}_{t2} + 60^o$, $\alpha_3 =\perp \boldsymbol{r}_{t3} + 60^o$. (b) $\alpha_i =\perp \boldsymbol{r}_{ti} + 60^o$.

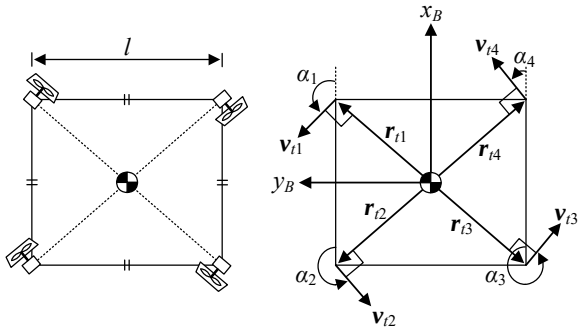

Figure 8: Four thrusters arranged in a square configuration.

a higher level of manipulability contributes to reducing energy consumption.

The aforementioned cases involve thruster arrangements in which the thruster angles are identical with respect to $\alpha_i =\perp \boldsymbol{r}_{ti}$. In addition, we examine w_t and $\Sigma||\boldsymbol{s}_t||$ for the case $\alpha_1 =\perp \boldsymbol{r}_{t1}$, $\alpha_2 =\perp \boldsymbol{r}_{t2} + 60^o$, $\alpha_3 =\perp \boldsymbol{r}_{t3} + 60^o$ with a path angle of $\theta_p = 20^o$; here, the direction angle of the first thruster differs from those of the second and third thrusters. We obtained w_t =0.0833 and $\Sigma||\boldsymbol{s}_t||$ =767.9838. The maneuverabilty is the same as in the case $\alpha_i =\perp \boldsymbol{r}_{ti} + 60^o$; however, the sum of the vector norms of the thruster speeds is larger. Computing the singular value decomposition of J_t, we can obtain $\Sigma_t = \mathrm{diag}(0.7644, 0.4298, 0.2537)$. The rotational maeuverability increases because $\alpha_1 =\perp \boldsymbol{r}_{t1}$; however, the maeuverability associated with the *x*-axis decreases. This explains why $\Sigma||\boldsymbol{s}_t||$ is greater than in the case $\alpha_i =\perp \boldsymbol{r}_{ti} + 60^o$. **Figure 7** illustrates the thruster speeds $\boldsymbol{s}_t$ when the vehicle perfectly tracks the straight line. We know that a larger value of s_{t3} is required to maintain the desired forward speed and heading angle; because $\alpha_1 =\perp \boldsymbol{r}_{t1}$ can generate a larger rotational motion, s_{t3} must compensate for this effect to maintain straight-line tracking. From this example, we observe that energy consumption can differ even when the maneuverability is the same. This is because the maneuverability is defined as the product of the singular values associated with the linear and rotational velocities, and different combinations of singular values can yield the same product.

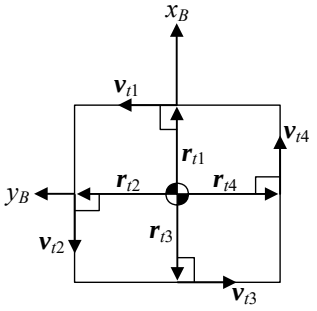

Figure 9: Thruster arrangement when $\alpha_i =\perp \boldsymbol{r}_{ti}$ and the length of the position vector $\boldsymbol{r}_{ti}$ is shorter than that in the case shown in **Figure 8**. The position vectors are given by $\boldsymbol{r}_{t1} = (\frac{l}{2}\ \ 0)^T$, $\boldsymbol{r}_{t2} = (0\ \ \frac{l}{2})^T$, $\boldsymbol{r}_{t3} = (-\frac{l}{2}\ \ 0)^T$, and $\boldsymbol{r}_{t4} = (0\ \ -\frac{l}{2})^T$.

4.2 Using Four Thrusters

Figure 8 shows a square arrangement formed by four thrusters. Let $l = 1$ m, and $\boldsymbol{r}_{t1} = (\frac{l}{2}\ \ \frac{l}{2})^T$, $\boldsymbol{r}_{t2} = (-\frac{l}{2}\ \ \frac{l}{2})^T$, $\boldsymbol{r}_{t3} = (-\frac{l}{2}\ -\frac{l}{2})^T$, $\boldsymbol{r}_{t4} = (\frac{l}{2}\ -\frac{l}{2})^T$. We investigate the maneuverability of the following three cases: (i) $\alpha_i =\perp \boldsymbol{r}_{ti}$ ($\alpha_1 = 135^o$, $\alpha_2 = -135^o$, $\alpha_3 = -45^o$, and $\alpha_4 = 45^o$); (ii)

$\alpha_i = \perp \boldsymbol{r}_{ti} \pm 30^o$; (iii) $\alpha_i = \perp \boldsymbol{r}_{ti} \pm 45^o$, and the Jacobian matrix J_t is given by

$$J_t = B_t^{\#} E_t \in \Re^{3\times 4} \tag{21}$$

$$B_t = \begin{pmatrix} I_2 & E\boldsymbol{r}_{t1} \\ I_2 & E\boldsymbol{r}_{t2} \\ I_2 & E\boldsymbol{r}_{t3} \\ I_2 & E\boldsymbol{r}_{t4} \end{pmatrix} \in \Re^{8\times 3} \tag{22}$$

$$E_t = \begin{pmatrix} \boldsymbol{e}_{t1} & \mathbf{0} & \mathbf{0} & \mathbf{0} \\ \mathbf{0} & \boldsymbol{e}_{t2} & \mathbf{0} & \mathbf{0} \\ \mathbf{0} & \mathbf{0} & \boldsymbol{e}_{t3} & \mathbf{0} \\ \mathbf{0} & \mathbf{0} & \mathbf{0} & \boldsymbol{e}_{t4} \end{pmatrix} \in \Re^{8\times 4} \tag{23}$$

Table 3 shows the results. Similar to the cases in **Subsection 4.1**, the case $\alpha_i = \perp \boldsymbol{r}_{ti}$ yields the largest maneuverability, and the value decreases as the angle deviation increases. In addition, if we want to increase the maneuverability associated with the rotational velocity, the thrusters can be rearranged so that the lengths of $\boldsymbol{r}_{ti}$ become shorter (denoted by $\alpha_i = \perp \boldsymbol{r}_{ti}$ (shorter)). **Figure 9** illustrates such a thruster arrangement, and the far-right column of **Table 3** confirms that this configuration increases the maneuverability while reducing energy consumption compared with the case $\alpha_i = \perp \boldsymbol{r}_{ti}$.

5. Conclusion

In this paper, we discussed a maneuverability measure for underwater vehicles based on robotic manipulability. Through the formulation and numerical examples, we showed the following:

(1) Robotic manipulability can be successfully applied to evaluate the maneuverability of underwater vehicles.
(2) A higher level of manipulability contributes to reducing energy consumption during tracking a path.
(3) Energy consumption can differ even when the maneuverability is the same. This occurs because maneuverability is defined as the product of the singular values corresponding to the linear and rotational velocities, and multiple combinations of singular values can yield the same product. Consequently, a maneuverability value that is suitable for one task may not be suitable for another.

Our future work will involve conducting a detailed investigation of the issue described in (3) and extending the analysis to three-dimensional motion.

Acknowledgement

This work was supported by the Korea Maritime & Ocean University Research Fund in 2025.

Author Contributions

Conceptualization, J. -K. Choi; Methodology, J. -K. Choi; Validation, J. -K. Choi, H. Kondo, S. Nishida; Formal Analysis, J. -K. Choi; Investigation, J. -K. Choi; Resources, J. -K. Choi, H. Kondo, S. Nishida; Data curation, J. -K. Choi; Writing-Original Draft Preparation, J. -K. Choi; Writing-Review & Editing, J. -K. Choi, H. Kondo, S. Nishida; Visualization, J. -K. Choi; Supervision, J. -K. Choi; Project Administration, J. -K. Choi; Funding Acquisition, J. -K. Choi.

References

[1] A. Ito, H. Shiobara, M. Miller, H. Sugioka, J. Ojeda, C. Tassara, M. Shinohara, M. Kinoshita and H. Iwamori, "Long-term array observation by ocean bottom seismometers at the Chile Triple Junction," Journal of South American Earth Sciences, vol. 124, 104285, 2023.

[2] J. -K. Choi, T. Fukuba, H. Yamamoto, Y. Furushima, T. Miwa, and K. Kawaguchi, "Pinpoint and safe installation of a standalone seafloor observatory," Proceedings of IEEE/MTS Oceans, 2018.

[3] T. Yokobiki, J. -K. Choi, S. Nishida, H. Matsumoto, E. Araki, K. Kawaguchi, N. Takahashi and S. Kodaira, "Construction of DONET2," Techno-Ocean, pp. 435-438, 2016.

[4] J. Kasahara, T. Sato, H. Momma, and Y. Shirasaki, "A new approach to geophysical real-time measurements on a deep-sea floor using decommissioned submarine cables," Earh, Planets and Space, vol. 50, pp. 913-925, 1998.

[5] T. Yoshikawa, "Manipulability of robotic mechanisms," The International Journal of Robotics Research, vol. 4, no. 2, pp. 3-9, 1985.

[6] T. Yoshikawa, "Dynamic manipulability of robot manipulators," Transactions of the Society of Instrument and Control Engineers, vol. 21, no. 9, pp. 970-975, 1985. (in Japanese)

[7] Y. Tadokoro, T. Ibuki and M. Sampei, "Dynamic manipulability analysis and design optimization of a fully-actuated hexrotor UAV with symmetric-coplanar-tilted-rotor structure," Transactions of the Society of Instrument and Control Engineers, vol. 53, no. 8, pp. 480-489, 2017. (in Japanese)

[8] E. Topini, M. Pagliai, and B. Allotta, "Dynamic maneuverability analysis: A preliminary application on an autonomous underwater reconfigurable vehicle," Applied Sciences, vol. 11, no. 10, 4469, 2021.